Microfluid Nanofluid (2008) 4:331–342
DOI 10.1007/s10404-007-0189-9

RESEARCH PAPER

Unsteady flow behaviors in an obstacle-type valveless micropump by micro-PIV

H. J. Sheen · C. J. Hsu · T. H. Wu · C. C. Chang · H. C. Chu · C. Y. Yang · U. Lei

Received: 2 March 2007 / Accepted: 21 May 2007 / Published online: 28 June 2007

Abstract In this paper, a PZT micropump excited by amplified squarewave signals with various frequencies was used to study the transient flow behaviors in an obstacle-type valveless micropump. A micro-particle-image-velocimetry (micro-PIV) with an external trigger was developed to obtain flow fields at the outlet and around the obstacle with various phases in a cycle. In comparison with previous studies on the pump performance, such as pump pressure and volume flow rate, more detailed information about the pump was obtained. The velocity profiles and periodic sectional mean velocities exhibited the unsteady flow nature. The total net flow generation efficiency per cycle was obtained experimentally by integrating the phase-dependent velocities. The flow recirculation around the obstacle was observed and quantified to investigate the influence on the pump performance. The duration, circulation, and the size of the recirculation regions indicated that this flow behavior could enhance the flow-directing capability. These results are very useful for the design and improvement of obstacle-type valveless micropumps.

Keywords Valveless micropump · Externally triggered micro-PIV · Micro oscillating flow · Flow recirculation

H. J. Sheen (✉) · C. J. Hsu · T. H. Wu · C. C. Chang · H. C. Chu · U. Lei
Institute of Applied Mechanics, National Taiwan University, No. 1, Sec. 4, Roosevelt Road, Taipei 106, Taiwan, ROC
e-mail: sheenh@ntu.edu.tw

C. Y. Yang
Department of Automatic Control Engineering, Chungchou Institute of Technology, 6, Lane 2, Sec. 3, Shanchiao Rd.,Yuanlin, Changhua 51003, Taiwan, ROC

List of symbols

A_o	Area of grid cell (mm^2)
d	Diameter of a glass tube
d_p	Diameter of seeding particle (μm)
D_f	Diffusion coefficient (m^2/s)
h	Height of liquid in a glass tube
I	Fluid inductance ($Pa\ s^2/m^3$)
n	Radial oscillating frequency
n_o	Refraction ratio
NA	Numerical aperture
$\hat{\mathbf{Q}}$	Volume of flow rate (m^3/s)
r	Characteristic length of channel (μm)
R	Flow resistance ($Pa\ s/m^3$)
t	Specific time in a time period (s)
t_r	Response time of tracer particle (s)
T	Time of a period (s)
u_i	Velocity in x or y direction (mm/s)
U_o	Maximum velocity at each velocity profile (mm/s)
Wo	Womersley number
Y_o	Channel width (μm)
$\hat{\mathbf{Z}}$	Complex form of flow impedance ($Pa\ s/m^3$)

Greek alphabets

δz_o	Depth of correlation (μm)
$\Delta\hat{\mathbf{P}}$	Complex form of pressure drop (Pa)
Δt	Time interval between the laser pulses (s)
ε_i	Errors due to Brownian motion
Γ	Circulation (mm^2/s)
η	The flow-directing efficiency of a valveless flow rectifier
η_o	Flow rate ratio of pump/supply phases in a obstacle-type micropump
ξ_{diffuser}	Flow resistance coefficient in diffuser direction
ξ_{nozzle}	Flow resistance coefficient in nozzle direction

λ	Wavelength of exciting light source (nm)
μ_f	Viscosity of fluid (N s/m^2)
ν_f	Kinematic viscosity of fluid (m^2/s)
ρ_f	Density of fluid (kg/m^3)
ρ_p	Density of tracer particle (kg/m^3)
ω_z	Vorticity in z direction (1/s)
θ	Collection angle

1 Introduction

1.1 Valveless micropump

Micropumps are essential components in microfluidic systems and are widely used in biochemical, biomedical, and biological fields. Two categories, reciprocating and continuous flow micropumps, are classified according to the actuation principles (Woias 2005). In a reciprocating micropump, the flow motion is generated by the volume change of the pump chamber. The net volume of fluid is obtained when the flow is directed by a rectifier like a valve or a flow-directing element. However, the fatigue of the valve and switching control may have adverse effects on the pump's performance and reliability. Therefore, valveless, or fixed-valve, micropumps have been proposed in recent years.

A type of valveless pump actuated by PZT membranes utilizes nozzle/diffuser elements to provide the direction-dependent flow resistance (Stemme and Stemme 1993; Olsson et al. 1995). Two nozzle/diffuser elements are connected to the pump chamber upstream and downstream, respectively. The pump cycle is divided into two modes, pump and supply modes. For smaller conical (opening) angles (less than 10°) of the nozzle/diffuser elements, lower flow resistance is obtained in the diffuser (diverging) direction than in the nozzle (converging) direction. Higher flow rate and the net flow thus exist in the diffuser direction. This diffuser element is also employed in a PMMA valveless micropump with electromagnetic actuation (Yamahata et al. 2005). Similar principle is used to fabricate the dynamic passive valve of another valveless pump (Gerlach and Wurmus 1995). This diffuser-valve is produced by anisotropic etching on a <100> silicon wafer. However, smaller flow resistance exists in converging direction due to a large aperture angle (around 70°), and consequently the net flow is in nozzle direction. The no-moving-parts valves, designed based on the Tesla-type planar structures, also possess rectification capability (Forster et al. 1995). The pressure pulses, which are the sudden jumps of the pressure amplitude, at the inlets and the outlets are reduced so that the pump efficiencies are increased. A trapezoid obstacle is placed along the centerline of the channel to form two equivalent planar nozzle/diffuser regions (Yang et al. 2003; Lee et al. 2005). The photos of the devices and the schematic diagrams of the pumping principle are shown in Fig. 1a. The obstacle-type flow rectifier (opening angle 7°) also provides the direction-dependent flow resistance, and the net flow rate is in the diverging direction.

1.2 Characterization of the valveless flow rectifiers and the flow fields

Many theoretical analyses and numerical simulations have been conducted to study the relation between the flow-directing capabilities and the direction-dependent flow resistance. A coefficient for characterizing the flow resistance can be defined as:

$$\xi = \frac{\Delta P}{\rho_f u_x^2/2} \tag{1}$$

where the pressure drop, ΔP, along the flow rectifier is influenced apparently by the valve geometries. The flow resistance coefficient and the time-dependent chamber volume are used to calculate the flow rates and pump pressure, respectively, with different arrangements of the pump chambers (Ullmann 1998).

In order to have a better prediction of the flow resistance, not only the friction factor but also the geometry effects such as expansion and contraction of the nozzle/diffuser valve are considered (Jiang et al. 1998; Olsson et al. 1999). The flow-directing capability of the valveless flow rectifier is defined by the ratio of resistance coefficient in the converging direction to that in the diverging direction as

$$\eta = \frac{\xi_{\text{nozzle}}}{\xi_{\text{diffuser}}} \tag{2}$$

The value of η is always larger than 1 for the diffuser element with a smaller opening angle so that volume flow rates are higher in the diverging direction.

In order to study the unsteady effects on the flow behaviors, not only flow resistance but also flow inductance needs to be considered. A typical expression of flow impedance in complex form is given as follows. It shows that impedance is mainly affected by flow resistance and pressure oscillating frequency (Morris and Forster 2003, 2004).

$$\hat{\mathbf{Z}} = \frac{\Delta\hat{\mathbf{P}}}{\hat{\mathbf{Q}}} = R + inI \tag{3}$$

The flow fields in the reciprocating type micropumps are very complex. Exact solutions of flow velocities in relation

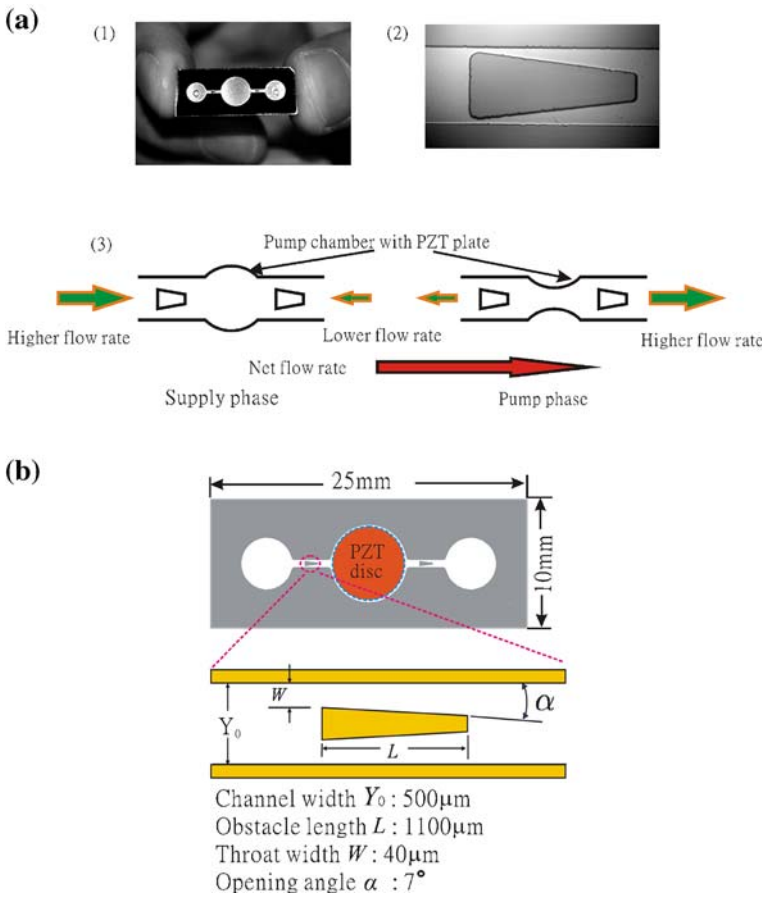

Fig. 1 **a** The photographs of (*1*) obstacle-type micropump, (*2*) the obstacle structure, and (*3*) the schematic diagram of the pumping principle. **b** The schematic diagram and dimensions of the obstacle-type PZT valveless micropump

to harmonic pressure gradients in a macroscale circular pipe (Womersley 1955; Uchida 1956) and a rectangular duct (Fan and Chao 1965) are derived from the Navier–Stokes equations. For an oscillatory flow, the pressure gradient is only a function of time and is usually expressed in the form of the Fourier series or Euler formula. From the momentum equation, the velocity which is a function of position and time is derived based on the time-dependent pressure gradient. Therefore, a phase-lag may exist between the flow velocity and the pressure gradient. In order to compare the transient initial force to the viscous force, one dimensionless parameter, Womersley number (Wo), is used to qualitatively identify quasi-steady flow behavior (Loudon and Tordesilla 1998).

$$\mathrm{Wo} = r\sqrt{\frac{n}{v_f}} \tag{4}$$

A quasi-steady flow is a flow in which the flow rate keeps up with a rapidly changing pressure gradient and is observed for Wo < 1. However, the phase-lag between the flow velocity and the pressure gradient can be observed when Wo is larger than 1. In addition, the velocity profile is different from that of a steady flow for Wo >> 1. For instance, parabolic-shape velocity profile no longer exists when the flow oscillates in a circular tube with Wo = 10 (Uchida 1956). The maximum velocity at the profile no longer occurs in the central region but in the region close to the channel wall. In a recent study, these unsteady flow natures in microchannels are also investigated numerically by using molecular dynamic simulation with different temperatures and densities (Hansen and Ottesen 2006).

1.3 Motivations and objectives

Pump pressures and volume flow rates are the most commonly used indices to describe the global performances in the literature (Olsson et al. 1995; Ullmann 1998; Gamboa et al. 2006). The flow fields around the valveless flow rectifiers, which carry useful information for pump design, have been investigated only in numerical simulations. The objective of the present paper is thus to provide experimentally measured flow field so that the actual pump characteristics may be assessed. A micro-PIV (micro-Particle-Image-Velocimetry) is employed for 2D full-field flow measurements. This technique has been widely utilized since it is proposed in 1998 (Santiago et al. 1998). For example, the measurements of blood flow (Park et al.

2003; Okuda et al. 2003), two-fluid flow with different refractive indices (Kim et al. 2004), counter current flow (Shinohara et al. 2004), and flow field in a fluidic oscillator (Yang et al. 2006) have all been obtained using this method. In addition, the data of the velocity vectors can also be used to evaluate the pressure fields in laminar channel flows by solving the Poisson equation (Fujisawa et al. 2006).

Measuring high-frequency oscillating flow in a micropump is difficult because the sampling rates of commercial PIV systems are merely around 15–20 Hz. In order to observe the instantaneous flow behavior, such as the transition at the moment of phase switch, an externally triggered signal with a particular phase-lock is incorporated in the present micro-PIV system. This technique is successfully used to demonstrate the oscillating flow in a triple-channel separator (Lee et al. 2007) and in a self-pumping micromixer (Sheen et al. 2007). With this improved micro-PIV system, the present results may yield more useful data for optimizing the pumping performance in the future design.

2 Experimental methods

2.1 Design and fabrication

The obstacle-type valveless flow rectifier under investigation was composed of two equivalent nozzle/diffuser regions between a symmetrical trapezoid obstacle and two side-walls, as shown in Fig. 1b. The opening angle of the nozzle/diffuser region was 7°. Two flow rectifiers were arranged in the upstream and the downstream channels of the pump chamber to provide the flow-directing capabilities. The flow-rectified principle is similar to that of the planar nozzle/diffuser valve with small opening angles. Therefore, lower flow resistance is expected when the fluids flow in the diverging direction. The dimensions of the microchannel were 500 μm in width and 50 μm in depth. The width of the throat and the exit of the diffuser region were 40 and 180 μm, respectively. The axial length of the obstacle was 1,130 μm. The diameter of the inlet and outlet cavities and the pump chamber were, respectively, 3 and 6 mm in diameter. An 8 mm-diameter circular PZT disc was attached on top of the silicon plate of the pump chamber to provide the volume expansion or compression. The dimensions of the obstacles in the micropump are also illustrated in Fig. 1b. The device was 25 mm in length, 10 mm in width, and 1 mm in thickness.

The fabrication process of the micropump was quite simple. A single polished silicon wafer <100> with a thickness of 500 μm was used in the production of the micropump. The photoresist AZ-P4620 was spun on the cleaned wafer, and only one photomask was required for the photolithography step. An inductive-couple-plasma (ICP) etcher, suitable for high aspect ratio anisotropic etching was used after the patterns were exposed and developed. An additional advantage of this dry etching technique is that surface roughness can be reduced. The microchannels were encapsulated by anodic bonding of a silicon wafer to the glass (Pyrex 7740) with thickness of 500 μm when the glass plate was given a DC voltage of 800 V at 400°C. The holes drilled at the inlet and the outlet on the silicon wafer were connected by the glass tubes with an inner diameter of 1.25 mm.

These levels of the fluids in the glass tubes varied according to the excitation conditions. Therefore, the pump pressure can be obtained by measuring the level difference between the inlet and the outlet. In addition, the flow rate can be evaluated easily as follows.

$$\dot{Q} = \frac{\pi}{4}\frac{d^2 \mathrm{d}h}{\mathrm{d}t} \tag{5}$$

Where $\dot{Q}$ is the measured flow rate, d is the diameter of the glass tubes, dh is the liquid-level difference between the inlet and the outlet, and dt is the time interval.

2.2 Measurements

A micro-PIV instrument with an external trigger function was used in the experiment so that a sufficient number of image pairs at the same phase could be acquired to evaluate the ensemble-averaged velocity field. Fluorescent particles (diameter 700 nm, Duke Scientific^{TM}) with an excitation peak at 542 nm and emission peak at 612 nm were chosen as the tracer particles. The fluorescent particles were diluted with depleted ion water to serve as the working fluids (particle concentration 0.25%). The density and dynamic viscosity of the They were excited by an Nd-YAG (New Wave^{TM}) double-pulsed laser with a wavelength of 532 nm. The laser pulses were expanded and transmitted into an inverted microscope (Nikon^{TM}) through a liquid-light-guide. The pulse energy density was thus reduced to protect the reflected mirrors inside the microscope. Uniform illumination was obtained when the incident light was transmitted along the light axis of the object lens. The fluorescence emissions of tracer particles were collected by a 20 X (NA = 0.5) object lens. A low pass filter (605 nm) was used to filter shorter wavelength emissions so that the background noise was reduced. The illuminated particle images were captured by a high-sensitivity 12-bit CCD (1600 × 1200 pixels resolution) which was mounted on the microscope.

A test micropump was mounted on an experiment holder which kept the focal plane and the chip in parallel. A double-channel function generator (HP^{TM}) provided the excitation and the trigger signals which were corrected with a reference phase. The square wave excitation signals amplified by a power amplifier were used to drive the PZT plate. The conditions of amplified voltages adopted here were 15–40 V (peak to peak) with frequencies ranging from 0.1 to 5 kHz. Moreover, the trigger signals, which were adjusted to a specified constant time delay with respect to the driving sources, were transmitted to a synchronizer via a cable. The synchronizer was used as a timing and control module in the micro-PIV system. The time solution of the synchronizer is 10^{-9} s, which is much shorter than 0.001% of the cycling period. The flow was illuminated by the laser pulses and the image pairs acquired by the CCD were processed in quick order right after the synchronizer received the externally triggered signals. One hundred pairs of images (frame A and frame B) were acquired and processed for each particular phase to raise the signal to noise ratio. The flow fields measured in the plane at the central depth of channel were used to calculate the velocity vectors by cross-correlation algorithm with Nyquist condition. Two regions, at the outlet and around the first obstacle, were chosen to measure the flow velocities. A digital camcorder was used to monitor the variations of flow rate and pump pressure. The arrangements of the instruments and the measuring regions are given in Fig. 2.

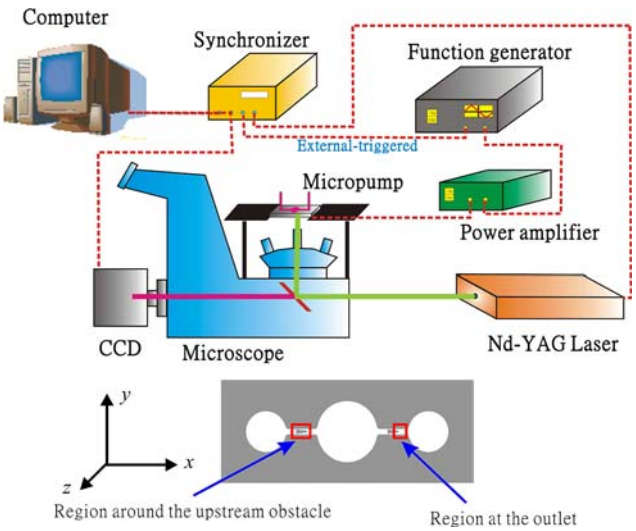

Fig. 2 Schematic diagrams of the instruments. The function generator provided both driving voltages and phase-locked trigger signals to the power amplifier and the synchronizer, respectively. Micropump was fixed on the holder and actuated by the amplified square-wave voltages from the power amplifier. The actions of laser and CCD were assigned by the synchronizer after receiving the externally triggered signal with specific phase. All digital image pairs were stored in the computer and used to evaluate velocity vectors. Two measuring regions are also exhibited in the figure

The interrogation window size chosen here was 16 × 16 pixels. According to the Nyquist condition, the in-plane vector resolution was determined as 6.8 μm × 6.8 μm. The out-of-plane spatial resolution, or the depth-of-correlation, is related to light diffraction, optical geometry of device, and particle sizes (Meinhart et al. 2000).

$$\delta z_o = \frac{3n_o\lambda}{NA^2} + \frac{2.16d_p}{\tan\theta} + d_p \tag{6}$$

While δz_o was estimated to be 9.5 μm, that is, 19% of the microchannel depth in the experiments. Although the 20 X object lens cannot provide high resolution in the out-of-plane direction due to the optical limitation, the larger view field still exhibited the global flow characteristics near the central plane.

In order to obtain the correct flow fields, the particle sizes and the particle dynamics should be considered (Devasenathipathy et al. 2003). The particle sizes used here were less than 1% of the hydraulic diameter of the channel. Moreover, the response time of the tracer particles should be far shorter than the cycling period. Based on a simple first-order inertial response to a constant flow, the equation of particle response time can be expressed as

$$t_r = \frac{d_p^2\rho_p}{18\mu_f} \tag{7}$$

The particle density and the dynamic viscosity of water are 1.05 g/cm^3 and 1.002 × 10^{-3} N s/m^2 (at 20°C), respectively. Therefore, the response time of a 700 nm polymer particle is less than 10^{-7} s.

Brownian motion, which is a temperature-dependent random motion, in a two-dimensional measurement was also considered as follows

$$\varepsilon_i = \frac{1}{u_i}\sqrt{\frac{2D_f}{\Delta t}} \tag{8}$$

where the subscript i indicates the x- or y-component. The selection of time interval Δt between frame A and B was varied according to the phase-dependent flow velocity in a period. A longer time interval was chosen for lower instantaneous flow velocity to reduce Brownian errors. For instance, the minimum velocity occurred at the phase switch and the time interval was set to be 200 μs. However, a shorter interval, 5 μs, was required especially when the maximum flow velocity appeared. A suitable adjustment of time interval was important in the measurement because of the instantaneous phase-dependent flow. The Brownian error was thus controlled to be less than 1% for all results in a cycle.

3 Results and discussion

3.1 Preliminary tests of the obstacle-type micropump

Preliminary tests of the micropumps provided the suitable conditions under which subsequent flow field measurements in the following sections were carried out. The pump performance was mainly dependent on the frequencies and voltages of the excitation signals for the same obstacle geometry. The pump pressures and volume flow rates with various operating conditions were measured by recording the variations of the liquid columns in the glass tubes.

Figure 3a shows the variation of the flow rates within the working frequency range from 1 to 3 kHz while the voltage was 30 V (peak to peak). A maximum pump output appeared at the optimal frequency, 1.9 k Hz. The rapidly nonlinear decay of volume flow rate was also presented when the input frequency was shifted away from the optimal frequency. The peak indicated that the maximum flow rate was 28.4 μl/min. Higher excitation voltages induced more pump outputs and extended the operation frequency ranges. In order to keep the reliability of the pump for the preliminary tests and the flow measurements, higher excitation voltages (>40 V) were not used here to prevent the damage of the PZT plate.

The characteristic diagram of the pump pressure and volume flow rate at 1.1, 1.5, and 1.9 kHz is given in Fig. 3b. The data did not indicate the maximum pump pressure at 1.5 and 1.9 kHz directly because the glass tubes at the outlet were too short to record the variation of the liquid level. The maximum pump pressure was estimated by a linear fitting to be about 1,100 Pa, when the PZT plate was excited with the signal of 30 V and 1.9 kHz. The volume flow rate was found to increase linearly with the voltages from 15 to 40 V at the resonance frequency as illustrated in Fig. 4. The critical voltage at which the fluid could be driven was estimated to be 12.5 V by a linear fit.

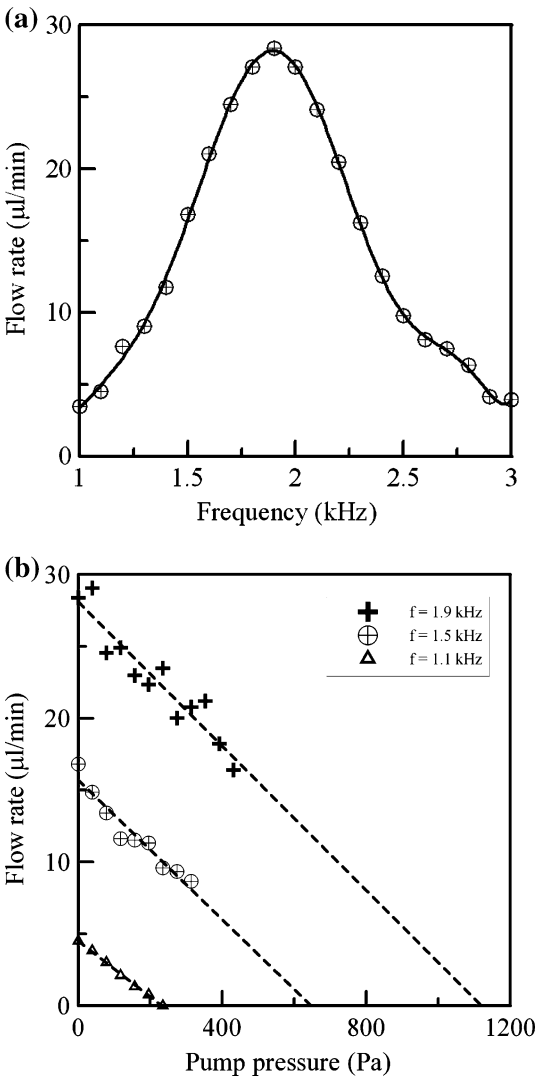

Fig. 3 The distribution of flow rates versus various frequency inputs (squarewave, 30 V peak to peak). The maximum flow rate was 28.4 μl/min at 1.9 kHz

3.2 Flows at the outlet

The unsteady flow field in the *x*–*y* plane was successfully measured by the externally triggered micro-PIV. The phase-dependent sectional mean velocities at the outlet in a cycle for 0.1, 1, 1.9, 3 k, and 5 kHz, are shown in Fig. 5. The first-half period corresponds to the pump phase (positive velocity) when 30 V was applied to the PZT plate and the second-half period to the supply phase (negative

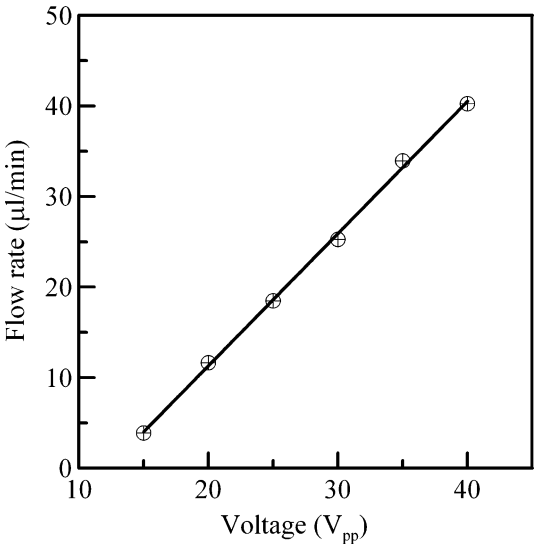

Fig. 4 The flow rates were found to be directly proportional to the input voltages (squarewave, 1.9 kHz)

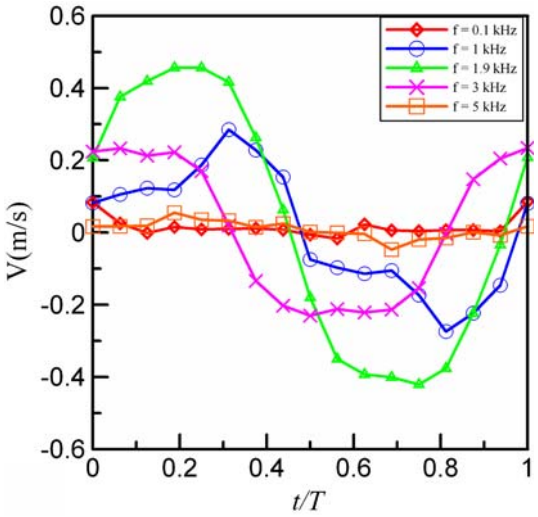

Fig. 5 The time-dependent mean sectional velocities at the outlet with various frequency inputs, 0.1, 1, 1.9, 3, and 5 kHz

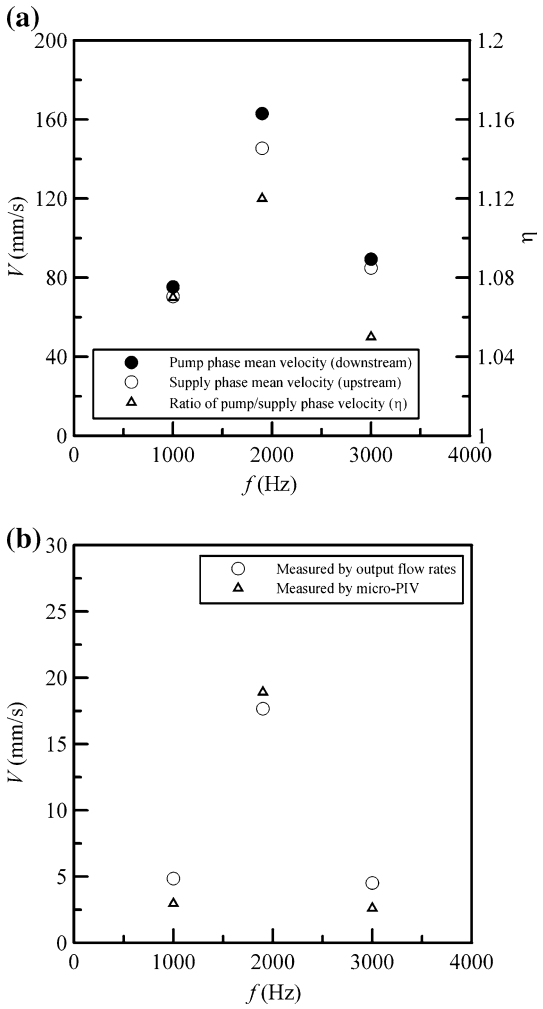

Fig. 6 **a** The pump and supply phase velocities, and the ratio of the pump/supply (downstream/upstream) velocities, **b** the comparison of the measured velocity in two different ways: by micro-PIV and by the output volume flow rates

velocity) when –30 V was applied. The flow motions decayed rapidly at the lowest excitation frequency of 0.1 kHz. The apparent flow velocities only appeared in the downstream direction at the initial pump phase. However, low flow velocities were also observed at the highest excitation frequency of 5 kHz, which might be caused by the increasing flow impedance.

Higher velocities appeared within the actuated frequency range between 1 and 3 kHz. The maximum velocity was obtained for 1.9 kHz, which was almost twice as large as those for 1 and 3 kHz. Although the variation of pressure gradient in the pump was not measured in this experiment, the phase-shifts of the velocity amplitudes were expected as the frequency increased. The velocity amplitudes in the pump phase were slightly higher than those in the supply phase, i.e. more volume of flow was transported toward the downstream direction. The direction of the net flow velocity in a cycle was verified by summing the phase-dependent velocities.

Figure 6a shows the pump and supply phase mean flow velocities obtained from the integrated results in Fig. 5. The ratios of pump/supply phase (downstream/upstream) flow velocities per cycle, η_o, indicated the global flow-rectified performances of the obstacle-type micropump. The results show that the maximum η_o, 1.12, was at the frequency of 1.9 kHz. The comparison of the net flow velocities by two different measuring methods are given in Fig. 6b. The results obtained by micro-PIV measurement were in good agreement with those by evaluating the net flow rate in the glass tube.

The velocity fields were also affected by the excitation frequencies. Table 1 lists Wo numbers for the chosen frequencies based on the hydraulic radius of the microchannel. The dimensionless velocity profiles in x–y plane at the outlet with frequencies of 1, 1.9, and 3 kHz are illustrated in Fig. 7. For this unsteady flow experiment, the maximum velocity no longer appeared in the central region, but close to the side-wall. The time-dependent distributions consistently show a decrease of velocity from the boundary layer to the central region. These phenomena were apparently observed when the pump and supply phases were switched. The velocity profiles also revealed the phase-shift manner when the frequency was increased to 3 kHz. Although the velocity profiles in the out-of-plane direction were not

Table 1 Womersley number for various frequencies

f (Hz)	100	1,000	1,900	3,000	5,000
Wo	0.54	1.7	2.3	2.9	3.8

Hydraulic radius = 22.7 μm

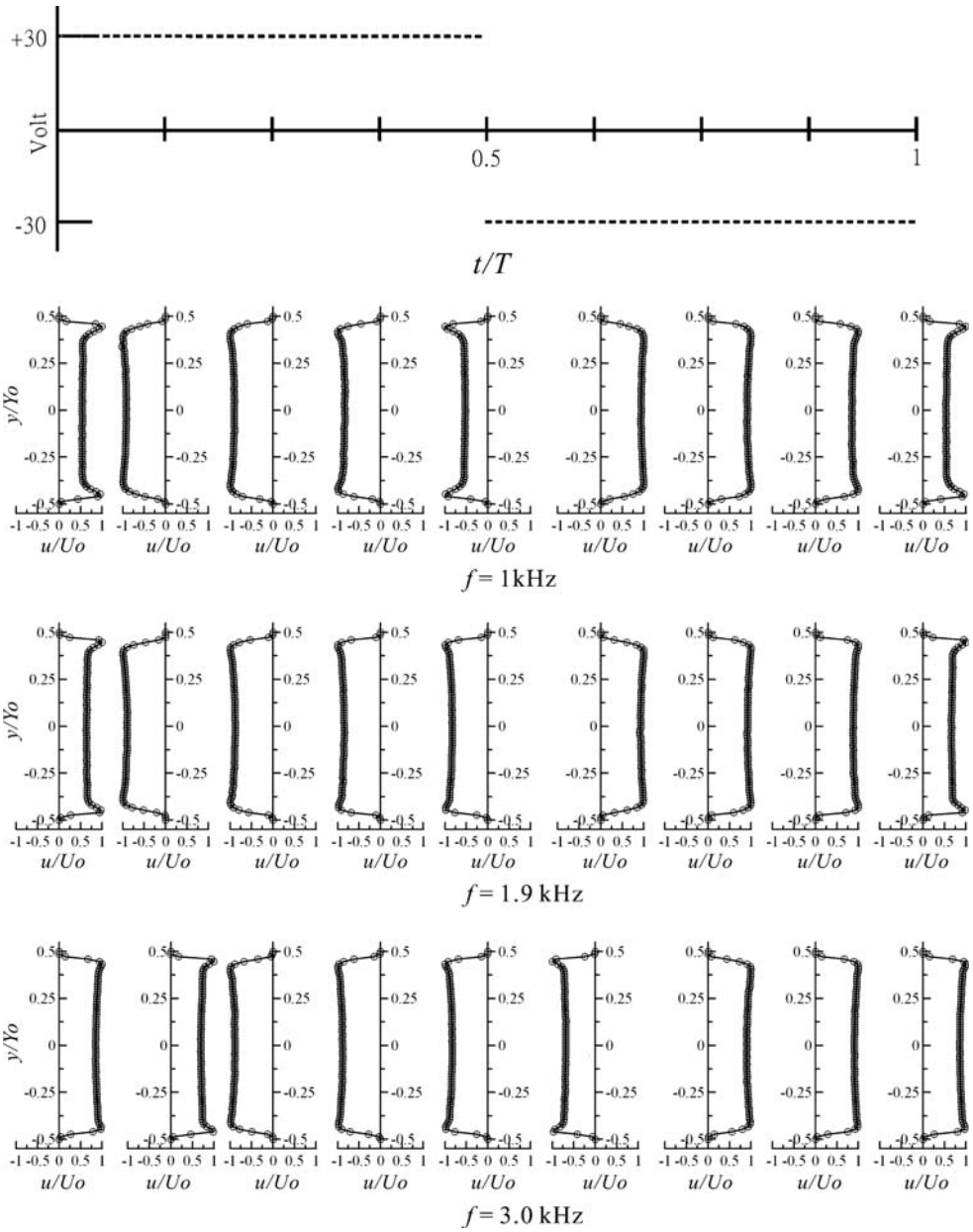

Fig. 7 The time-dependent velocity profiles at the outlet with various frequency inputs, 1, 1.9, and 3 kHz

measured due to the resolution of depth correlation, similar velocity distributions should occur along the z direction. In summary, the higher flow velocities were present near the boundaries of the rectangular channel, whereas the lower velocities existed in the central region.

3.3 Flow around the obstacle

The flow fields around the obstacle-type rectifier upstream the chamber was more complex than those at the outlet. Three typical flow patterns were experimentally observed within a time period and can be classified as (I) pump phase smooth flow, (II) flow recirculation, and (III) supply phase smooth flow. Figure 8a–j shows the evolution of the time-dependent velocity vectors (upper part of the figure) and the streamtrace patterns (lower part) upstream the throat of the diffuser region at the optimal frequency. The streamtraces could be regarded as the typical streamlines in the 2D flow fields, which were used to visualize the flow fields. The Reynolds numbers in Fig. 8 were evaluated based on the hydraulic diameter of the throat. The maximum *Re* was about 115, i.e. in the range of laminar flow.

Figure 8a shows the velocity vectors and streamtraces at the end of the supply phase (t = –2/32 T). The velocity decreased and the flow changed from toward downstream to upstream direction when the supply phase was switched to the pump phase. The velocity vectors also display that the higher velocities were near the side-wall, whereas the

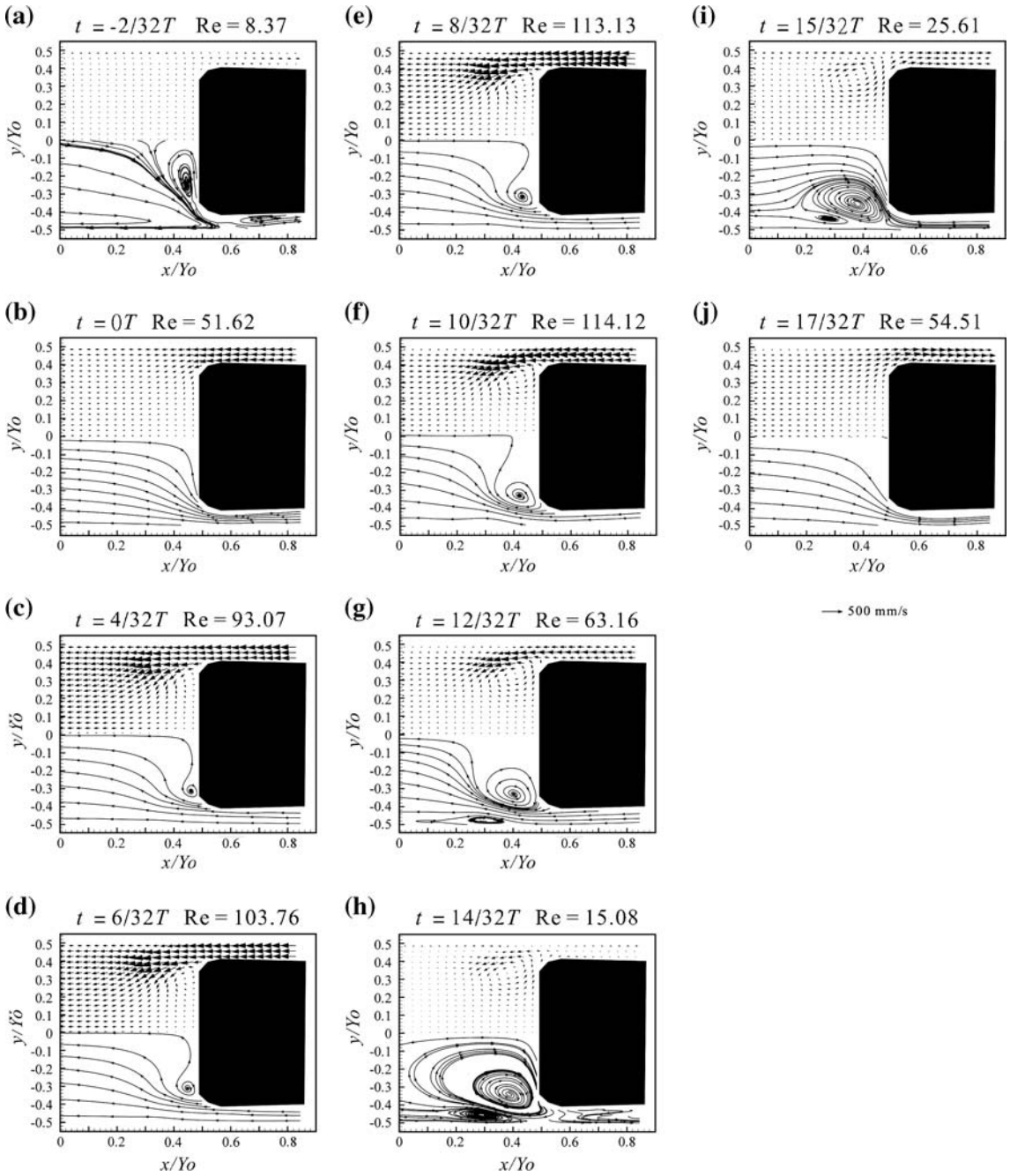

Fig. 8 The time-dependent flow fields including velocity vectors (*upper half*) and streamtraces (*lower half*) upstream of the valve throat

lower velocities were in the central region. Flow recirculation was generated due to the significant velocity gradient and was clearly exhibited by the streamtrace. The recirculation disappeared soon after and the flow became smooth when the fluids were accelerated at $t = 0$ T as given in Fig. 8b.

As t was increased, the pump phase smooth flow patterns remained qualitatively unchanged from 0 to 2/32T. However, flow recirculation emanated at $x/Y_o = 0.45$, $y/Y_o = \pm 0.3$ and was observed at 4/32 T in Fig. 8c. The upper fluids rotated counterclockwise, whereas the lower fluids rotated clockwise. A recirculation zone was generated and then enlarged gradually in the latter half period of the pump phase. A recirculation bubble formed at 8/32 T and the size of recirculation bubble increased during the interval between 10/32 and 14/32 T as depicted in Fig. 8d–h. Two pairs of flow recirculation zones, a primary one and a secondary one, appeared and the vorticity in the secondary recirculation zones was opposite to the primary one. At the next phase as shown in Fig. 8i, the flow penetrated the re-

circulation bubble and then the primary recirculation region shrank. A closed recirculation was observed and was replaced by the pump phase smooth flow thereafter. Figure 8j illustrates the supply phase smooth flow. The fluids were drawn towards the chamber from t = 17/32 to 30/32 T.

Figure 9 reveals the flow evolution downstream the first obstacle. The flow patterns were similar to those in Fig. 8, but shorter durations and smaller sizes of the recirculation regions were observed. The flow became chaotic in the time period before the switches of the pump and the supply phases at t = –2/32 T and 15/32 T. The flow patterns are shown in Fig. 9a, c. Some flow recirculations with smaller sizes were observed between the obstacle and the side-wall. On the other hand, the flows were smooth most of the time in the pump and supply phases as illustrated in Fig. 9b, d, respectively.

In order to further investigate the rotating motion, vorticity, which represents the strength of flow rotation, should be calculated first. The vorticity, ω_z, is related by the gradient of axial velocity in the radial direction.

$$\omega_z = \frac{\partial v}{\partial x} - \frac{\partial u}{\partial y} \tag{9}$$

The positive and negative values mean the counterclockwise and clockwise rotations, respectively. The durations, the rotation strength, and the recirculation size were all evaluated based on the vorticity fields and the streamtrace patterns in the experiment. Circulation, an integration of the absolute value of vorticity in recirculation region, was used as an index for the rotation strength. A 20% cut-off-value of the vorticity was chosen to exclude the random vorticity fluctuation in the recirculation region.

$$\Gamma = A_0 \sum_{i \in \text{recirculation}} \omega_i \tag{10}$$

Figure 10a–c reveals the duration, circulation, and size of the recirculation regions around the obstacle-type rectifier in a time period with frequencies of 1, 1.9, and 3 kHz. The durations of recirculation regions caused by the reversed flow upstream are indicated by the solid symbols and downstream by the hollow symbols. From the phase-dependent mean velocities in Fig. 6 and the durations in Fig. 10a, the results show that the flow recirculation appeared at the end of pump or supply phase. The duration depended on the excitation voltages, frequencies, and the geometries of the obstacle-type rectifier. When a laminar flow moved through the sudden expansion at the throat or exit of the diffuser region, the flow separation easily occurred due to the adverse pressure gradient.

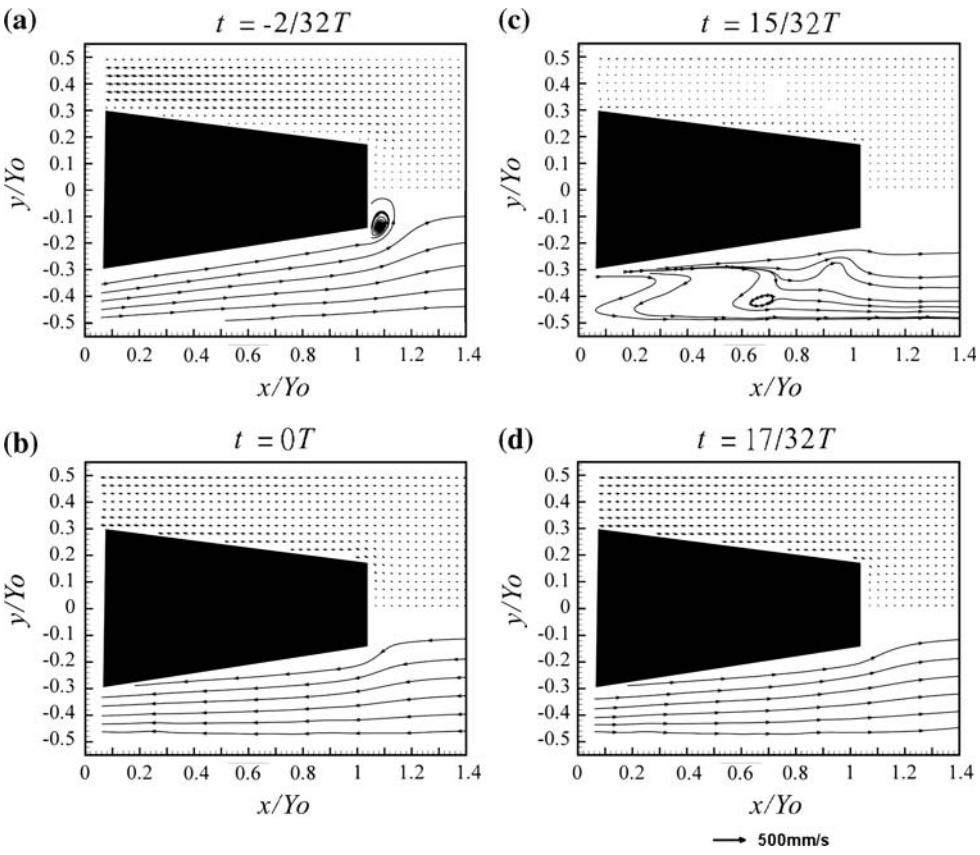

Fig. 9 The time-dependent flow fields including velocity vectors (*upper half*) and streamtraces (*lower half*) downstream of the valve throat

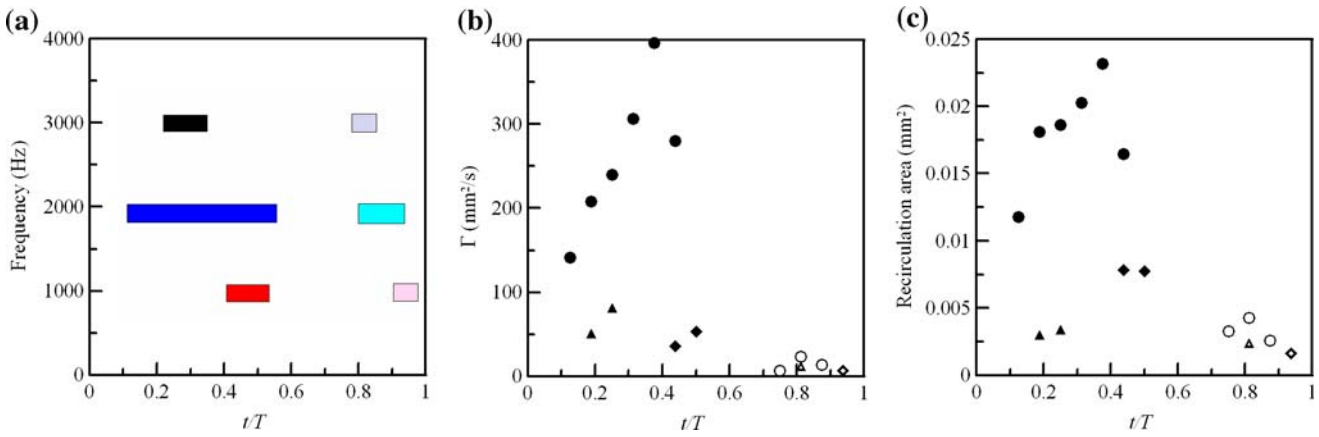

Fig. 10 The **a** duration, **b** circulation, and **c** size of the recirculation regions measured upstream of the throat (*deeper colors* or *solid symbols*) and the downstream regions (*lighter colors* or *hollow symbols*) of the obstacle-type valve. Three excitation frequencies were used here, 1 kHz (*diamond symbol*), 1.9 kHz (*circle symbol*), and 3 kHz (*triangle symbol*)

Figure 10b, c shows the circulation and area of the recirculation regions, which are in agreement with the flow patterns in Figs. 8 and 9. The solid symbols represents the circulation and size of recirculation regions caused by the reversed flow upstream the obstacle, while the hollow ones indicate the results downstream. The experimental results also indicated that the strength and size of the recirculation region were dependent on the excitation frequency. When the pump was actuated at the optimal frequency, the fluids had the largest kinetic energy. Although the kinetic energy was dissipated by the viscous force, the fluids near the recirculation region were disturbed so that the strength and size were increased with increasing time. In summary the flow recirculation became more pronounced when a flow with a higher velocity moved through a sudden expansion with a higher area ratio. This effect led to stronger rotation and larger size upstream the obstacle where the reversed flow moved through the throat at the optimal frequency. A large-scale recirculation region can also be attained by increasing the excitation voltage.

In the present experiment, no clear relationship was found between these properties and the related *Re* numbers. For example, the maximum circulation and the size of the recirculation at the optimal frequency appeared at $t = 14/32\ T$ while the highest *Re* number was 114.1 at $t = 10/32\ T$. However, these results revealed that the pressure drag caused by the flow recirculation could not be neglected when the fluids flowed through the rectifier. Higher pressure drop of the flow would result in larger recirculation region. Therefore, the reversed flow had more pressure drag than the forward one. This phenomenon was favorable to flow-directing capability of this obstacle-type flow rectifier. The same flow behaviors were also observed around the second obstacle, which were half-period phase shift with respect to those around the first one.

The aforementioned results showed that not only the diffuser element but also the flow recirculation had influences on the direction-dependent flow resistance. In order to reduce the flow resistance caused by the recirculation of the forward flow, the trapezoid obstacle can be replaced by a triangular one. In a further study, this technique will be used to investigate the flow resistance and the efficiency of net flow generation for various geometry designs of the obstacles in order to optimize the pump performance.

4 Conclusions

An externally triggered micro-PIV system was successfully used to measure the full-field flow in an obstacle-type PZT valveless micropump. The nature of the high-frequency periodic unsteady flow was clearly explored in this experiment. The quantitative measurements provide significant insights into the flow behaviors, which are critical for the improvement of the performance of the micropump. Based on the test cases presented, the following conclusions may be drawn:

(1) The pump could only be actuated within a certain excitation frequency range from 1 to 3 kHz. The maximum output volume flow rate appeared at the resonance frequency of 1.9 kHz, at which the highest instantaneous velocity was also measured.
(2) The phase-shifts between the sectional mean velocities and the excitation voltages were obtained when Wo > 1. In addition, due to the high-frequency oscillating flows, the annular-shape velocity profiles were found to exist in both the *x*–*y* and *x*–*z* planes.
(3) The instantaneous flow velocities in the pump and the supply phases were one or two order higher than the net flow velocity. The ratio of pump/supply phases

volume flow rates, η_o, which is important for the improvement of the reciprocating-type pump performance, was successfully evaluated in this experiment.

(4) The measured velocity vectors and flow patterns indicated that the flow fields became complex when the oscillating flows passed through the obstacle-type valve. The sudden expansion geometries at the valve throat and exit enhance due to the velocity gradient in the radial direction and the flow recirculation was thus induced. The duration, rotation strength, and size of the flow recirculation were evaluated to investigate their effects on the flow-rectified capabilities.

(5) The pressure losses induced by the recirculation regions were direction-dependent. The evolution of the flow recirculation indicated that the obstacle-type valve provided more flow resistances when in the reverse flow direction. This flow phenomenon enhanced the flow-directing capability of the present obstacle-type valve.

Acknowledgments This work was supported by Ministry of Economic Affairs, 96-EC-17-A-05-A1-0017, and National Science Council of Taiwan, NSC 95-2218-E-002-051-MY3, R.O.C.

References

Devesenathipathy S, Santiago JG, Wereley CD, Meinhart CD, Takehara K (2003) Particle imaging techniques for microfabricated fluidic systems. Exp Fluids 34:504–514

Fan C, Chao BT (1965) Unsteady, laminar, incompressible flow through rectangular ducts. ZAMP 16:351–60

Forster FK, Bardell RL, Afromowitz MA, Sharma NR, Blanchard A (1995) Design, fabrication and testing of a fixed-valve micropump. IMECE FED 234:39–44

Fujisawa N, Nakamura Y, Matsuura A F, Sato Y (2006) Pressure field evaluation in microchannel junction flows through μPIV measurement. J Microfluid Nanofluidics 2:447–453

Gamboa AR, Morris CJ, Forster FK (2006) Improvements in fixed-valve micropump performance through shape optimization of valves. J Fluids Eng 127:339–346

Gerlach T, Wurmus H (1995) Working principle and performance of the dynamic micropump. Sens Actuators A 50:135–140

Hansen JS, Ottesen JT (2006) Molecular dynamic simulations of oscillatory flows in microfluidic channel. J Microfluid Nanofluidics 2:301–307

Jiang XN, Zhou ZY, Huang XY, Li Y, Yang Y, Liu CY (1998) Micronozzle/diffuser flow and its application in micro valveless pumps. Sens Actuators A 70:81–87

Kim BJ, Liu YZ, Sung HJ (2004) Micro PIV measurement of two-fluid flow with different refractive indices. Meas Sci Technol 15:1097–1103

Lee CJ, Tu ZK, Lei U, Hsu CJ, Sheen HJ (2005) A valveless micropump with asymmetric obstacles. In: 16th international symposium on transport phenomena, Prague

Lee CJ, Sheen HJ, Chu HC, Hsu CJ, Wu TH (2007) The development of a triple-channel separator for particle removal with self-pumping oscillating flow. J Micromech Microeng 17:439–446

Loudon C, Tordesillas A (1998) The use of the dimensionless Womersley number to characterize the unsteady nature of internal flow. J Theor Biol 191:63–78

Meinhart CD, Wereley ST, Gray MHB (2000) Volume Illumination for two-dimensional particle image velocimetry. Meas Sci Technol 11:809–814

Morris CJ, Forster FK (2003) Low-order modeling of resonance for fixed-valve micropumps based on first principles. J MEMS 12:325–334

Morris CJ, Forster FK (2004) Oscillatory flow in microchannels—comparison of exact and approximate impedance models with experiments. Exp fluids 36:928–937

Okuda R, Sugii Y, Okamoto K (2003) Velocity-field measurement of in vitro blood flow using micro PIV technique. In: 5th internal symposium on particle image velocimetry, paper:3315

Olsson A, Stemme G, Stemme E (1995) A valve-less planar fluid pump with two pump chambers. Sens Actuators A 46–47:549–556

Olsson A, Stemme G, Stemme E (1999) A numerical design study of the valveless diffuser pump using a lumped-mass model. J Micromech Microeng 9:34–44

Park CW, Lee SJ (2003) Micro-PIV measurements of blood flow in a micro-channel. In: 5th internal symposium on particle image velocimetry, paper: 3314

Santiago JG, Werely ST, Meinhart CD, Beebe DJ, Adrian RJ (1998) A particle image velocimetry system for microfludics. Exp Fluids 25:316–319

Sheen HJ, Hsu CJ, Wu TH, Chang CC, Chu HC, Yang CY, Lei U (2007) Experimental study of flow characteristics and mixing performance in a PZT self-pumping micromixer. Sens Actuators A (in press)

Shinohara K, Sugii Y, Aota A, Hibara A, Yokeshi M, Kitamori T, Okamoto K (2004) High-speed micro-PIV measurement flow in microfluidic devices. Meas Sci Technol 15:1965–1970

Stemme E, Stemme G (1993) A valve-less diffuser/nozzle based fluid pump. Sens Actuators A 39:159–167

Uchida S (1956) The pulsating viscous flow superposed on the steady laminar motion of incompressible fluid in a circular pipe. ZAMP 7:403–422

Ullmann A (1998) The piezoelectric valve-less pump—performance enhancement analysis. Sens Actuators A 69:97–105

Woias P (2005) Micropumps—past, progress and future prospects. Sens Actuators B 105:28–38

Womersley RJ (1955) Method for the calculation of velocity, rate of flow and viscous drag in arteries when the pressure gradient is known. J Physiol 127:553–563

Yamahata C, Lotto C, Al-Assaf A, Gijs M A M (2005) A PMMA valveless micropump using electromagnetic actuation. J Microfluid Nanofluidics 1:197–207

Yang CY, Lin JD, and Lei U (2003) A valve-less micro-pump based on asymmetric obstacles. In: 7th Taiwan NEMS/MEMS conference, pp 330–333

Yang JT, Chen CK, Tsai KJ, Lin WZ, Sheen HJ (2006) A novel fluidic oscillator incorporating step-shaped attachment walls. Sens Actuators A (in press)